

Theoretical investigation of direct and phonon-assisted tunneling currents in InAlGaAs/InGaAs bulk and quantum-well interband tunnel junctions for multijunction solar cells

U. Aeberhard

IEK5-Photovoltaik, Forschungszentrum Jülich, 52425 Jülich, Germany

(Received 28 September 2012; revised manuscript received 7 January 2013; published 5 February 2013)

Direct and phonon-assisted tunneling currents in InAlGaAs-InGaAs bulk and double-quantum-well interband tunnel heterojunctions are simulated rigorously using the nonequilibrium Green's function formalism for coherent and dissipative quantum transport in combination with a simple two-band tight-binding model for the electronic structure. A realistic band profile and the associated built-in electrostatic field are obtained via self-consistent coupling of the transport formalism to Poisson's equation. The model reproduces experimentally observed features in the current-voltage characteristics of the devices, such as the pronounced current enhancement in the quantum-well junction as compared to the bulk junction and the structure appearing in the negative-differential resistance regime due to quantization of emitter states. Local maps of density of states and the current spectrum reveal the impact of quasibound states, electric fields, and electron-phonon scattering on the interband tunneling current. In this way, resonances appearing in the current through the double-quantum-well structure in the negative-differential resistance regime can be related to the alignment of subbands in the coupled quantum wells.

DOI: [10.1103/PhysRevB.87.081302](https://doi.org/10.1103/PhysRevB.87.081302)

PACS number(s): 72.20.Dp, 73.40.Gk, 73.40.Kp, 88.40.jp

Interband tunnel junctions (TJs) are essential components in multijunction solar cell devices, allowing for the series connection of single junction subcells with different band gaps as used for an enhanced utilization of the solar spectrum.^{1,2} In a recent publication, the use of a double-quantum-well (DQW) structure in the junction region was shown to enhance considerably the peak tunneling current in an InAlGaAs-InGaAs TJ, at moderate loss of transparency.³ For a proper analysis of the potential of this approach and to enable further optimization of the junction design, an accurate and comprehensive theoretical description of the physical processes involved in the transport is required. However, conventional models for tunnel junctions as used for the simulation of multijunction solar cells are usually limited in this respect by a large number of simplifying assumptions on the density of states participating in the tunneling, the occupation of these states, and the assisting scattering mechanisms.^{4,5}

In this Rapid Communication, the tunnel junction is simulated using a rigorous quantum transport approach based on the nonequilibrium Green's function (NEGF) formalism as used in the nanoelectronics community for the simulation of interband tunneling transistors.⁶⁻¹⁰ In combination with atomistic electronic structure theory and self-consistent coupling to a Poisson solver, the approach is able to provide a realistic picture of the relevant density of states and associated current flow under nonequilibrium conditions, by accurately reflecting the effects of internal fields, carrier confinement, and elastic as well as inelastic scattering mechanisms.

The present approach is based on the implementation of the NEGF formalism for III-V quantum-well (QW) structures with photovoltaic applications as introduced in Ref. 11, with the material parameters of the nearest-neighbor two-band tight-binding (TB) model and interactions adjusted to the InAlGaAs-InGaAs system of Ref. 3, as presented in Table I. The orbital basis, contrary to a band basis such as $\mathbf{k} \cdot \mathbf{p}$, enables a consistent and unified description of electrons independent of their position in energy with respect to conduction and valence

bands and is thus ideally suited for interband tunneling processes. The TB parameters are adjusted to reproduce the zone center band gaps and effective masses of the bulk component materials, choosing the light hole mass (due to higher tunneling probability) for the description of the valence band. The width of the model layer, consisting of cation and anion sublayers, amounts to half the lattice constant of the layer material. Homogeneous meshes are used for energy and momentum, with energy resolution $\Delta E = 5$ meV and momentum grid size $N_k = 25$. The TB parameters at the interfaces are treated as in Ref. 12. Among the various existing scattering mechanisms for electrons and holes, elastic coupling to acoustic phonons is considered within the deformation potential approximation, and the inelastic interaction with polar optical phonons is included via the corresponding Fröhlich Hamiltonian, with parameters also displayed in Table I. While the former process results in a broadening of the spectral quantities in both the energy and transverse momentum domains, the latter is essential for the description of the phonon mediated tunneling current at vanishing overlap of electron and hole states in the injector regions. At the present stage, no trap-assisted tunneling relying on additional defect states is included, which potentially leads to an underestimation of the dark interband current, especially at higher forward bias voltages. Together with the use of an oversimplified band structure model ignoring any effects of lattice mismatch and the absence of realistic contact losses, this precludes a fully quantitative analysis and restricts the discussion to qualitative features.

The device structures under consideration are displayed in Fig. 1 and correspond to the central region of the devices discussed in Ref. 3. The tunnel junction consists of two adjacent 15 nm thick layers of $\text{In}_{0.52}\text{Al}_{0.33}\text{Ga}_{0.15}\text{As}$ with a high doping level of $N_{d/a} = 10^{19} \text{ cm}^{-3}$. In the DQW structure, 8 nm of $\text{In}_{0.53}\text{Ga}_{0.47}\text{As}$ are inserted on each side of the junction to form the potential wells leading to a local constriction of the interband tunneling barrier. For the present simulation, the size of the lightly doped ($N_{d/a} = 2 \times 10^{17} \text{ cm}^{-3}$) buffer layers on

TABLE I. Material parameters used in simulations.

	InAlGaAs	InGaAs	
E_s (eV)	1.04	0.74	s -orbital on-site energy
E_p (eV)	-0.14	0.0	p_z -orbital on-site energy
V_{sp} (eV)	2.54	2.6	Layer coupling element
m_{el}^*/m_0	0.065	0.041	Effective electron mass
m_{hh}^*/m_0	0.087	0.052	Effective hole mass
ϵ_r	13.2	14.2	Static dielectric constant
ϵ_∞	10.7	11.0	High-frequency dielectric constant
$\hbar\Omega_{LO}$ (eV)	0.038	0.033	Optical phonon energy
D_{ac} (eV)	5	5	Acoustic deformation potential

top and bottom of the tunnel junction is reduced to 30 nm, and neither the p -doped InGaAs capping layer nor the n -doped InP substrate present in the original structures are included.

The equilibrium band edge profiles and associated local density of states (LDOS) at a vanishing transverse momentum ($\mathbf{k}_\parallel = 0$) corresponding to the above layer structures and doping levels are shown in Fig. 2, with the equilibrium Fermi level fixed at 1 eV. In the bulk heterojunction case, displayed in Fig. 2(a), the strong band bending close to the junction results in the appearance of bound states in both electron and hole emitter regions. While these states feed the tunneling current, they are themselves not accessible from the contacts without energy relaxation. Hence, there is only a vanishingly narrow forward bias regime with a finite energetic overlap of bulk electrode states at the low doping levels of the n^+ and p^+ regions, where ballistic transport from one contact to the other via exclusively direct tunneling in the junction region is possible, in spite of the lower band gap at the n contact. As a consequence, any description based on a ballistic picture of direct tunneling will severely underestimate current flow even close to zero bias. There is, however, an extended forward bias regime with a finite energetic overlap of interface states close to the junction via which the tunneling can proceed. In the DQW case, displayed in Fig. 2(b), both the energetic overlap

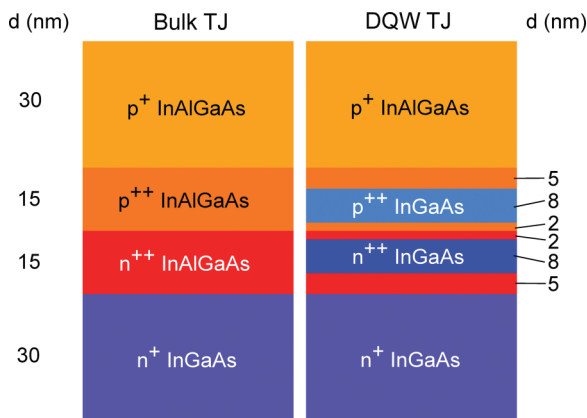


FIG. 1. (Color online) Schematic layer and material structure of the bulk and DQW tunnel-heterojunction devices from Ref. 3. The doping density amounts to $N_{d/a} = 2 \times 10^{17} \text{ cm}^{-3}$ for the lightly doped n^+/p^+ regions and $N_{d/a} = 10^{19} \text{ cm}^{-3}$ for the heavy n^{++}/p^{++} doping.

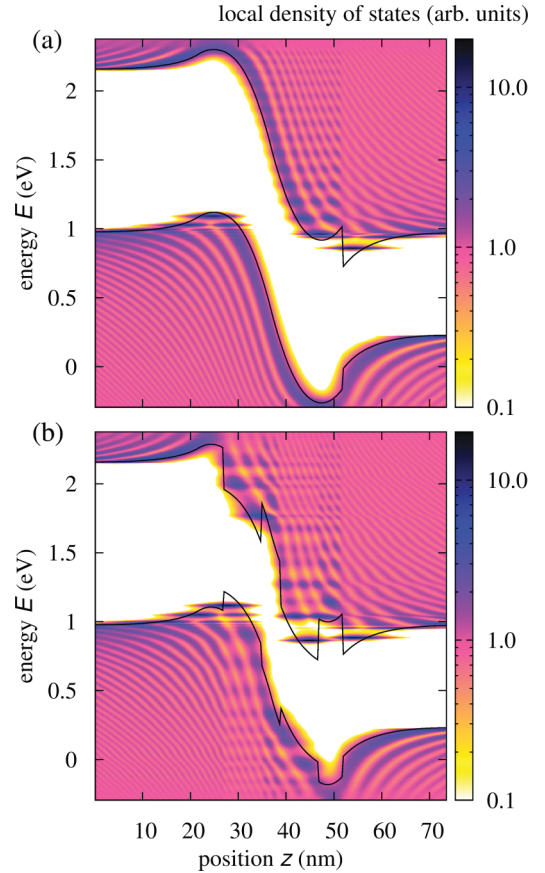


FIG. 2. (Color online) Band profile and local density of states at a vanishing transverse momentum and zero bias voltage, for (a) the bulk heterojunction device, exhibiting state quantization in the highly doped emitter regions adjacent to the junction, and (b) the DQW heterojunction device, where the strong band bending leads to the unbinding of the high-lying confined states. The equilibrium Fermi level is fixed at 1 eV.

and spatial extension of interface states is increased due to the presence of the additional confined subgap states in the quasi-two-dimensional (2D) QW regions close to the junction. The extremely strong band bending results in a partial unbinding of the higher QW states, such that the LDOS is no longer well described by the states of a square well potential, but rather a new confinement potential reflecting the effects of both band bending and band offsets. In combination with the confined states at the heterojunction interface, the injector regions thus provide a complex combination of bound, quasibound, and continuum states participating in the interband tunneling process.

Figure 3 displays the current-voltage characteristics of the interband charge transport in the bulk and DQW heterojunctions as computed with the NEGF model. The current-voltage characteristics reproduce the qualitative features of the experimental data in Ref. 3 in terms of a significantly higher peak current and peak voltage, resulting from the lower effective barrier potential, but lower negative-differential resistance (NDR) for the DQW TJ as compared to the bulk TJ. As can be inferred from Fig. 2(a), the structure appearing in the NDR region of the I - V characteristics for the bulk

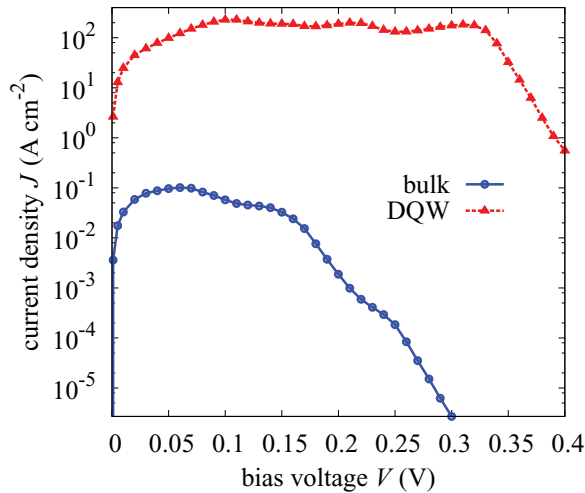


FIG. 3. (Color online) Current-voltage characteristics of bulk and DQW heterojunction devices at forward bias. Due to the lower effective barrier potential, the peak current in the DQW device exceeds that of the bulk junction by more than two orders of magnitude and occurs at a much larger bias voltage. The structure in the negative-differential resistance regime exhibited by the bulk device can be ascribed to the quasi-2D state quantization in the emitter regions adjacent to the junction, as shown in Fig. 2. The corresponding features in the I - V characteristics of the DQW heterojunction device are considerably stronger and are identified as the signatures of resonant tunneling between QW states.

heterojunction is due to discretization of the longitudinal DOS in the injection regions adjacent to the junction. In the DQW sample, the local current maxima are much more pronounced and are identified as the signatures of resonant tunneling between different QW states.

In order to analyze the current flow in the two structures in more detail with respect to the different extended and localized states involved, the current spectrum at a different bias voltage is computed for the full spatial extent of the device. The p -contact Fermi level remains fixed at 1 eV, while the n -contact Fermi level is shifted upwards by the applied bias voltage. In the case of the bulk heterojunction, the result displayed in Fig. 4, together with the corresponding LDOS ($\mathbf{k}_{\parallel} = 0$), allows the distinction of different regimes of interband charge transport depending on the applied bias: At the peak voltage of 0.06 V, as shown in Fig. 4(a), current flow is dominated by carriers first tunneling through the triangular barrier of the heterointerface at the electron contact into the lowest subband of the doping-induced potential well at the n side of the junction and then into the second subband of the doping-induced potential well at the p side, from where escape to the hole contact proceeds via electron-phonon scattering. A minor contribution is due to ballistic transport above the triangular barrier into the subband associated with the first localized state at the p side. At a bias of 0.16 V [Fig. 4(b)], after an initial relaxation close the contacts mediated by multiple scattering events with phonons, current flow proceeds again predominantly via tunneling through the triangular barrier from the n side, but now into the first subband of the doping-induced potential well at the p side; at an even

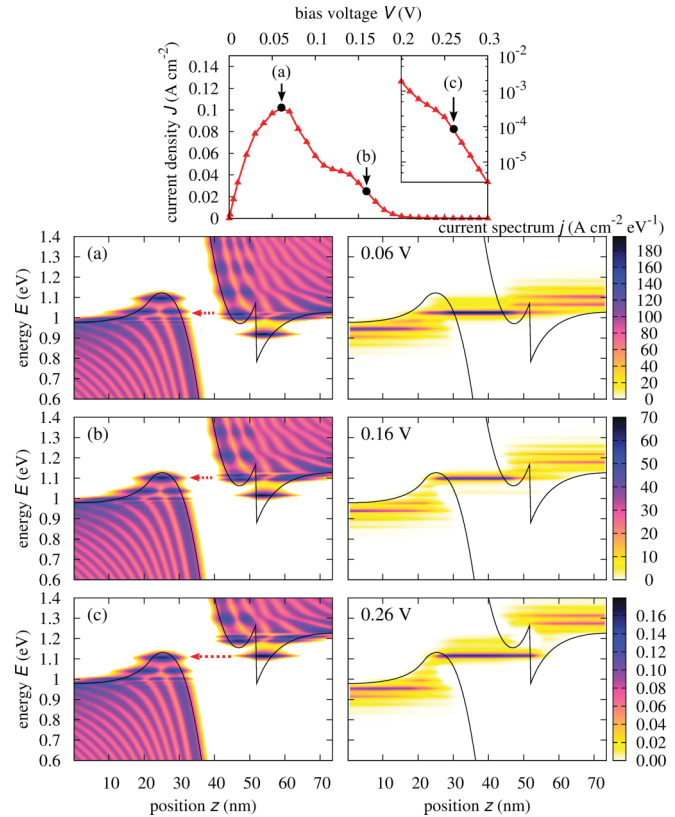


FIG. 4. (Color online) Current-voltage characteristics, local density of states, and the corresponding local current spectrum of the bulk tunnel-heterojunction device at forward bias voltages of (a) 0.06 V, (b) 0.16 V, and (c) 0.26 V, illustrating different interband tunneling processes depending on the energetic alignment of localized and extended states in the injection regions adjacent to the junction.

larger bias voltage of 0.26 V, displayed in Fig. 4(c), the major part of the current flows via the lowest subband of the triangular potential well at the heterointerface into the first subband at the p side, overcoming a substantially thicker tunneling barrier, while only a small fraction of carriers are transported via phonon-assisted tunneling from the higher interface states. Beyond this transport regime, i.e., for considerably larger separations of contact Fermi levels, there are no more available current paths in terms of energetically overlapping states in the injection regions, and current breaks down exponentially, until thermionic emission sets in, or, in more realistic cases, defect-assisted tunneling takes over. In the DQW TJ, as shown in Fig. 5, the dominant role in the transport process is played by the QW states, which, in the case of energetic alignment at specific values of the bias voltage, give rise to resonant tunneling. On the n side, current flow proceeds over the whole bias regime via tunneling into the second subband of the QW and subsequent relaxation into the lowest subband, while the states in the triangular well at the heterointerface seem to be irrelevant for transport. On the p side, there is a strong bias dependence of the specific subband involved in the interband tunneling process: At 0.16 V [Fig. 5(a)], the alignment is between the lowest subband at the n side and the third subband

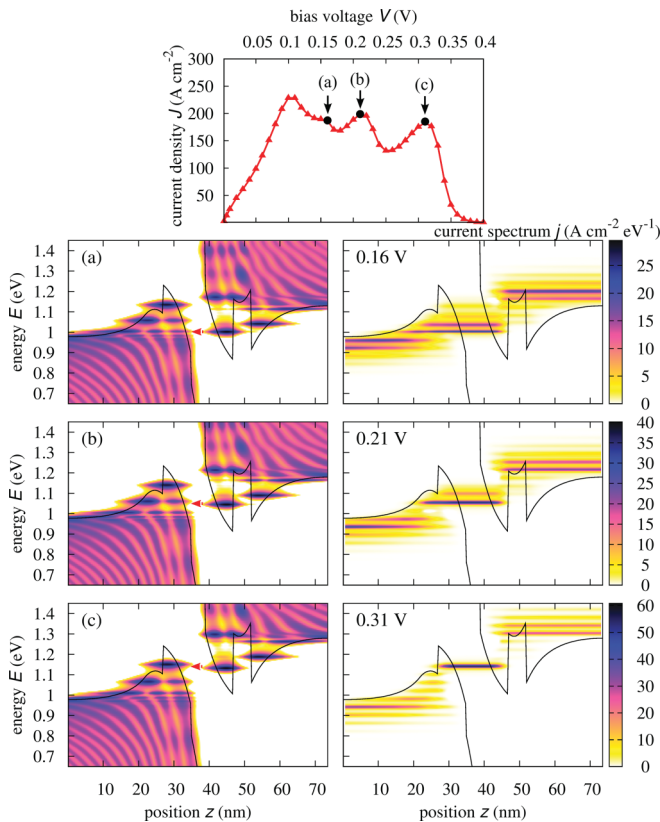


FIG. 5. (Color online) Current-voltage characteristics, local density of states, and the corresponding local current spectrum of the DQW tunnel-heterojunction device at forward bias voltages of (a) 0.16 V, (b) 0.21 V, and (c) 0.31 V, at which electrons tunnel resonantly from the lowest QW subband at the n side of the junction to the third, second, and first QW subband at the p side, respectively.

state at the p side, at 0.21 V [Fig. 5(b)], the second subband is resonant, and at 0.31 V [Fig. 5(c)], carriers are transferred between the first subbands of the QW. Again, beyond this point, energetic overlap is limited to phonon sidebands, which results in an exponential decay of the current with increasing forward bias voltage. Finally, in both tunnel junction devices, due to the prominent role of narrow bands with enhanced transmission, the current spectrum close to the contacts shows a pronounced structure depending on the phonon energy, in spite of the bulklike, continuous DOS in these regions.

In conclusion, we have presented a rigorous approach to the simulation of carrier transport in interband tunnel junctions with applications in multijunction solar cells, which is able to account for both direct and phonon-assisted contributions under consideration of realistic spatial potential variations, including arbitrarily shaped quantum-well structures. By consideration of the local maps of DOS and current spectrum, a microscopic picture of the current flow at different values of forward bias voltage is obtained. Apart from providing insight into the dominant transport mechanisms at a given bias, the simulation results are in qualitative agreement with the experimentally found large increase in peak current and peak voltage as well as a decrease of NDR by the insertion of a double-quantum-well structure in the junction region. The quantitative agreement of the tunneling currents with the measured values is expected to be improved by the use of a larger tight-binding basis such as $sp^3d^5s^*$,¹³ consideration of strain, a more accurate treatment of the scattering processes, and, most notably, the inclusion of defect-assisted tunneling processes. The latter is essential to extend the present approach to multijunction solar cell devices based on disordered and defect-rich materials, such as the micromorph silicon thin-film tandem solar cell.

¹M. Yamaguchi, T. Takamoto, K. Araki, and N. Ekins-Daukes, *Sol. Energy* **79**, 78 (2005).

²R. R. King, D. C. Law, K. M. Edmondson, C. M. Fetzer, G. S. Kinsey, H. Yoon, R. A. Sherif, and N. H. Karam, *Appl. Phys. Lett.* **90**, 183516 (2007).

³M. P. Lumb, M. K. Yakes, M. González, I. Vurgaftman, C. G. Bailey, R. Hoheisel, and R. J. Walters, *Appl. Phys. Lett.* **100**, 213907 (2012).

⁴M. Hermle, G. Létay, S. P. Philipps, and A. W. Bett, *Prog. Photovoltaics* **16**, 409 (2008).

⁵J. R. Hauser, Z. Carlin, and S. M. Bedair, *Appl. Phys. Lett.* **97**, 042111 (2010).

⁶M. Ogawa, R. Tominaga, and T. Miyoshi, in *International Conference on Simulation of Semiconductor Processes and Devices: SISPAD 2000* (IEEE, New York, 2000), p. 66.

⁷C. Rivas, R. Lake, G. Klimeck, W. R. Frensley, M. V. Fischetti, P. E. Thompson, S. L. Rommel, and P. R. Berger, *Appl. Phys. Lett.* **78**, 814 (2001).

⁸C. Rivas, R. Lake, W. R. Frensley, G. Klimeck, P. E. Thompson, K. D. Hobart, S. L. Rommel, and P. R. Berger, *J. Appl. Phys.* **94**, 5005 (2003).

⁹M. Luisier and G. Klimeck, *J. Appl. Phys.* **107**, 084507 (2010).

¹⁰J. Knoch and J. Appenzeller, *IEEE Electron Device Lett.* **31**, 305 (2010).

¹¹U. Aeberhard and R. H. Morf, *Phys. Rev. B* **77**, 125343 (2008).

¹²T. B. Boykin, *Phys. Rev. B* **54**, 7670 (1996).

¹³J. M. Jancu, R. Scholz, F. Beltram, and F. Bassani, *Phys. Rev. B* **57**, 6493 (1998).